Tribological behavior of TZ4YS-$MoSi_2$ composites obtained by Spark Plasma Sintering

Rut Benavente[1], María D. Salvador[1], Carlos Bloem[1], Carlos F. Gutiérrez-González[2], Carmen Alcázar[3], Rodrigo Moreno[3], Amparo Borrell[1]

[1]Instituto de Tecnología de Materiales (ITM). Universitat Politècnica de València, Camino de Vera, s/n, 46022 Valencia, Spain

[2]Nanoker Research S.L., Polígono Industrial Olloniego, Parcela 22A, nave 5. 33660, Oviedo, Spain

[3]Instituto de Cerámica y Vidrio (ICV), Consejo Superior de Investigaciones Científicas (CSIC), Kelsen 5, E-28049 Madrid

*Corresponding author: Instituto de Tecnología de Materiales (ITM), Universitat Politècnica de València, Camino de Vera s/n, 46022, Valencia, Spain. Tel.: +34645603843; Fax: +34963877629.

E-mail address: rutbmr@upvnet.upv.es

Abstract

The aim of this work was to evaluate the role of $MoSi_2$ content (5, 10, 15 wt%) in the mechanical and tribological behavior of TZ4YS-$MoSi_2$ composites obtained by colloidal processing and spark plasma sintering (SPS) at 1500ºC. Firstly, the densification of TZ4YS-$MoSi_2$ composite and the shrinkage-rate curves by SPS applying 80 MPa from 1300ºC to 1500ºC is studied. The hardness and fracture toughness values confirmed that up to 99.9% densification is gradually reached with increasing $MoSi_2$ percentage. Secondly, pin-on-disk tribological tests at different distances (1, 5, 15 and 2000 m) with Al_2O_3 as counterpart were performed to record the behavior of the materials in the initial and final stages of wear. The $MoSi_2$ content was associated to the beginning of the transition from mild to severe wear, higher

the amount of $MoSi_2$ faster is the transition. This behavior was correlated with $MoSi_2$ content, which aids the formation of a tribolayer.

Keywords: Zirconia; $MoSi_2$; Rheology; Spark Plasma Sintering; Wear

1. Introduction

Yttria stabilized zirconia (YSZ) is one of the most versatile ceramic materials due to its wide range of applications. One of the most important features lies on its spectacular mechanical properties desired for structural applications, with a compression resistance up to 2000 MPa due to a crystalline modification that opposes to the propagation of cracks [1]. The YSZ uses include ceramic bearings, valves, abrasive materials, knives, high temperature heating elements, bioceramics, thermal barriers and oxygen sensors, among others [2,3]. In particular, yttria-stabilized zirconia materials exhibit the highest strength (tensile strength up to 1200 MPa), of all single-phase oxide ceramics, and high toughness (up to 6 $MPa \cdot m^{1/2}$), although they can still suffer of slow crack growth and delayed fracture phenomenon [4].

Molybdenum disilicide ($MoSi_2$) is a hopeful structural material for use at high-temperature due to its high melt point (2020 °C) and superb oxidation resistance [5,6]. $MoSi_2$ seems to be a promising element for tribological applications, due to its high wear resistance at high-temperature [7]. Monolithic $MoSi_2$ material has been found to be exceptionally wear resistant in abrasive environments, with a wear mechanism similar to that of oxide ceramics. Moreover, the wear resistance of $MoSi_2$ can be further improved with the addition of second phases [7–10].

There are several papers reporting the effect of zirconia particles in a $MoSi_2$ matrix, which have demonstrated to improve the oxidation resistance of the non-oxide material allowing higher temperature of use. However, at the best of our knowledge, yttria-stabilized zirconia (YSZ) matrix composites reinforced with molybdenum disilicide ($MoSi_2$) particles are materials that

are barely studied at present [7]. These composites have a promising behavior at high temperature, and the addition of $MoSi_2$ as a second phase is expected to improve some mechanical properties of YSZ such as hardness, toughness, and wear behavior. In particular, the addition of $MoSi_2$ has been explored in zirconia-based thermal barrier coatings to promote a self-healing behavior produced by the oxidation of molybdenum and silicon that react at high temperature with atmospheric O_2 producing gaseous MoO_3 and solid SiO_2 [11,12].

In this context, in order to obtain YTZP/$MoSi_2$ ceramic composites with enhanced properties and increased reliability, it is imperative to control the physicochemical parameters of powders, avoiding the presence of agglomerates, to diminish defects in the sintered materials. This can be achieved by controlling the mixing of the components in the colloidal process as well as particles shape and size distribution and interparticle forces [13]. Another highly relevant aspect is the microstructural control in order to obtain fully dense materials [14].

Regardless of its potential interest, the development of ZrO_2-$MoSi_2$, or other composites such as ZrB_2-$MoSi_2$, ZrC-$MoSi_2$, SiC-$MoSi_2$, is, however, still incipient and, moreover, there is almost no information about their tribological behavior. Consequently, the present study aims to investigate the dry sliding wear behavior of ZrO_2-$MoSi_2$ composites obtained by aqueous colloidal processing of zirconia partially stabilized with yttria (4 mol%) and $MoSi_2$ mixtures, and subsequent spark plasma sintering (SPS).

2. Materials and Methods

2.1 Colloidal processing

The following raw materials were used as starting powders: 1) a commercial ZrO_2 doped with 4 mol% Y_2O_3 (TZ4YS, Tosoh, Japan) with a theoretical density of 6.05 $g \cdot cm^{-3}$, specific surface area of 7.0 $m^2 \cdot g^{-1}$ and 0.6 μm of average particle size, and 2) $MoSi_2$ (Grade C, HC Starck Advanced Ceramics, Germany), with a specific surface area of 1.4 $m^2 \cdot g^{-1}$ and an average particle size of 2.5 μm. Particle sizes were measured by laser diffraction (Mastersizer S,

Malvern, UK) and surface area was measured by one-point N_2 adsorption with a Monosorb Surface Area Analyser MS-13 (Quantachrome Co., USA).

The colloidal stability of the starting ceramic powders was studied independently through zeta potential measurements as a function of both the pH and the concentration of polyelectrolytes, in order to determine the optimum working pH and deflocculant concentration. Measurements were carried out using the laser Doppler principle in combination with non-invasive back-scattering (Zetasizer Nano-ZS, Malvern, UK). Aqueous slurries with a solids content of 0.1 $g \cdot L^{-1}$ were obtained using 10^{-2} M KCl as an inert electrolyte and by adjusting the pH values with 10^{-1} KOH and 10^{-1} HCl M solutions. Prior to the measurements the suspensions were dispersed with a sonication probe (UP 400S, Dr Hielscher GmbH, Germany) operated at a frequency of 24 kHz for 1 minute. The suspensions were maintained in an ice bath during sonication to avoid overheating. As for deflocculants, a poly(acrylic acid)-based polyelectrolyte (Duramax^{TM} D3005, Rohm & Haas, USA, with 35 wt% active matter) was used for TZ4YS, and a synthetic polyelectrolyte with unknown composition (Produkt KV5088, Zschimmer-Schwarz, Germany), which has proven its suitability for the dispersion of non-oxide ceramics, was used to disperse the $MoSi_2$ powders [15].

To maximize the solids concentration of the suspension while keeping very low viscosity values suitable for freeze-drying, suspensions were prepared with solids contents of 30 vol.% These suspensions were prepared always following the usual procedure, keeping the water at the desired deflocculant content by continuous mechanical stirring with propellers and then slowly addition of the TZ4YS powders. For suspensions which combined TZ4YS and $MoSi_2$, PKV was added to a previously dispersed aqueous suspension of TZ4YS, and then $MoSi_2$ powders were subsequently incorporated while maintaining mechanical stirring. The prepared compositions contained TZ4YS with 5, 10 and 15 wt.% $MoSi_2$ (compositions labeled as TZ5M, TZ10M and TZ15M, respectively).

The rheological characterization of the prepared suspensions was carried out using a rotational rheometer (MARS, Thermo Haake, Germany) with double-cone/plate sensor configuration with a

cone angle of 2º equipped with a solvent trap to prevent evaporation (DC60/2, Thermo Haake, Germany). The temperature was kept constant at 25 °C by means of a temperature water bath controller. The measuring program was carried out under controlled shear rate mode using a three-stage measuring cycle. The first stage was the linear increase of the shear rate from 0 to 1000 s^{-1} in 5 minutes, followed by a plateau at the maximum shear rate (1000 s^{-1}) for 1 minute, and the third stage was a decrease of the shear rate from 1000 to 0 s^{-1} in 5 minutes. Sonication was performed using several 1-minute cycles with a maximum sonication of 4 minutes, since further sonication cycles led to agglomeration.

After choosing the optimal conditions to achieve a stable and homogeneous suspension, the materials were put into volumetric flasks, which were connected to a rotary evaporator (120 rpm, RV10 basic, IKA, Germany) and frozen using a bath of liquid N_2. Then, the frozen suspensions were freeze-dried (Cryodos 50, Telstar, Spain) to sublimate the ice in the frozen material at a pressure of 5 Pa and a condenser operating temperature of -50 °C for 24 h. The powders thus obtained were sieved at a pressure of 5 Pa and a condenser temperature of -50 °C for 24 h. The powders obtained were sieved at a temperature of -50 °C. The powders obtained were sieved through a 63 µm mesh. The composite powders were also dissolved in aqueous suspensions which were then freeze-dried using the same methodology.

2.2 Densification and microstructural characterization

The dry powders were put into a graphite matrix with an inner diameter of 20 mm and fed into the spark plasma sintering apparatus HP D25/1 (FCT Systeme GmbH, Rauenstein, Germany) under low vacuum (1 Pa) for sintering at a temperature of 1500 ºC, which assured full densification. A uniaxial constant compacting pressure of 80 MPa was applied from the beginning of the sintering cycle. The tests were performed with a heating rate of 100 ºC·min^{-1} and 5 minutes of permanence at the maximum temperature.

The bulk density of the specimens was measured by the Archimedes method (ASTM C373-88) [16] with water as the immersion medium using densities of 6.05 and 6.26 $g \cdot cm^{-3}$ for TZ4YS and $MoSi_2$, respectively. The relative density was obtained by dividing the bulk density with the theoretical density of the powder mixture.

The crystalline phases of the powder and sintered bulk materials were determined by X-ray diffraction (XRD) with a D8 Advance diffractometer (Bruker, Karlsruhe, Germany) using Cu Kα radiation. The measurements were performed in the interval 10°-80°, and the step size and the reading time were 0.02º and 2 s, respectively.

The microstructure of fracture surfaces of sintered specimens was examined by field emission scanning electron microscopy (FESEM, S4800 Hitachi, Japan). The average grain sizes of the materials were calculated from FESEM images using the linear intersection method [21]. In addition, FESEM was connected to EDX (Energy-Dispersive X-ray spectroscopy) equipment (Oxford Instruments, Abingdon, UK) to carry out microanalysis of different features observed in the microstructure.

2.3 Mechanical properties

The hardness and fracture toughness of the materials were measured using an indentation technique. A conventional diamond pyramid indenter (Vickers) was fit to the piece of equipment (4124, Innovatest, Netherlands) and a load of 9.8 N was applied for 15 s in accordance to the standard specification ASTM E384-17 [17] [17]. To estimate the indentation fracture toughness K_{IC}, Vickers indentations with a load of 98 N were performed on the surface of the samples, inducing Palmqvist cracks, from which the indentation fracture toughness was obtained by the method of Niihara [18].

2.4 Tribological characterization

The friction test was performed under dry conditions on a Microtest MT2/60/SCM/T (Spain) tribometer. Pin-on-disk configuration was chosen according to ASTM G99–17 [19] [19]. The upper specimen (pin) ball of Al_2O_3 from Fritsch (Germany) with a hardness of 1820 HV_{30} and a radius of 3 mm. The lower specimen (disk) was made as aforementioned with SPS, TZ4YS composites with 5, 10 and 15 wt% $MoSi_2$ (20 mm in diameter and 5 mm in thickness) using 5 samples of each percentage of $MoSi_2$. The specimens were grinded up to grit 4000 with a roughness < 0.1 μm.

Prior to every wear test, the specimens and the ball were ultrasonically cleaned in an alcohol bath and allowed to dry. The test conditions were: 0.01 $m \cdot s^{-1}$ for sliding velocity, normal load of 15 N and sliding distance of 1, 5, 15 and 2000 m in air (relative humidity of 40–50%) at room temperature 20~22 °C without lubrication at 300 rpm.

The theorical contact area of ball – half space is given by Hertz contact theory where an elastic sphere of radius **R** indents an elastic half-space where total depth deformation is **d**, causing an initial contact area of radius **a**, which will vary upon subsequent sliding due to wear [20]:

$$a = \sqrt{(R \cdot d)} \tag{1}$$

d is related to the applied force **F**:

$$d = \sqrt[3]{\left(\frac{3 \cdot F}{4 \cdot E' \cdot \sqrt{R}}\right)^2} \tag{2}$$

$$E' = \frac{(1-\upsilon_1^2)}{E_1} + \frac{(1-\upsilon_2^2)}{E_2} \tag{3}$$

where E_1 and E_2 are the elastic moduli and ν_1 and ν_2 are the Poisson coefficients related with each material. So, the initial contact radius (**a**) in this configuration is 54.94 μm, and the initial contact width must be 109.88 μm. These values will vary upon subsequent sliding due to wear.

3. Results and discussion

3.1 Colloidal processing

The colloidal behavior of TZ4YS aqueous suspensions has been reported in earlier work [15] [15]. The isoelectric point occurs around pH 7 and decreases towards pH~3.2 with 0.2 wt% PAA addition and the zeta potential value at working pH is -53 mV, high enough to provide good stability. The dispersion of $MoSi_2$ was conferred using the deflocculant PKV5088. The isoelectric point occurs at pH 2. The variation of zeta potential as a function of PKV content is shown in Figure 1. As it can be seen the zeta potential varies from –26 mV without addition of deflocculant to -70 mV with 1.5 wt% PKV, and maintains constant for further contents. The curve of TZ4YS [15] [15] is also plotted to facilitate comparison. In this case the particle surfaces are positively charged without deflocculant (+16 mV) and become negative after the addition of PAA, with a zeta potential of -53 mV for 0.2 wt%.

Once the concentration of deflocculant for each component was selected, suspensions of the mixtures were prepared to a solids loading of 30 vol.% and optimizing the sonication time. Figure 2 shows the flow curves of mixtures containing 5, 10, and 15 wt% $MoSi_2$. Agitation with helices is not sufficient to provide stability, and therefore non sonicated slurries have a high viscosity and a broad thixotropy, demonstrating their lack of homogeneity. After 1 min sonication all samples exhibit a nearly Newtonian behavior with very low viscosities that maintain with further sonication. In Figure 2c the variation of viscosity (registered at 1000 s^{-1}) as a function of sonication time is plotted. In spite of the relatively high solids loading (30 vol.%) the viscosity is always extremely low although it seems to very slightly increase with the $MoSi_2$ content. Therefore, subsequent freeze drying of these slurries will lead to mixtures with high uniformity.

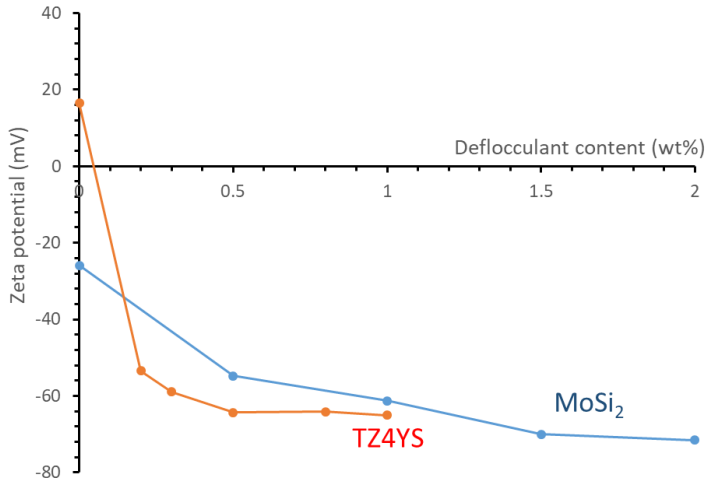

Figure 1. Variation of zeta potential with the concentration of deflocculant (PAA for TZ4YS and PKV for $MoSi_2$).

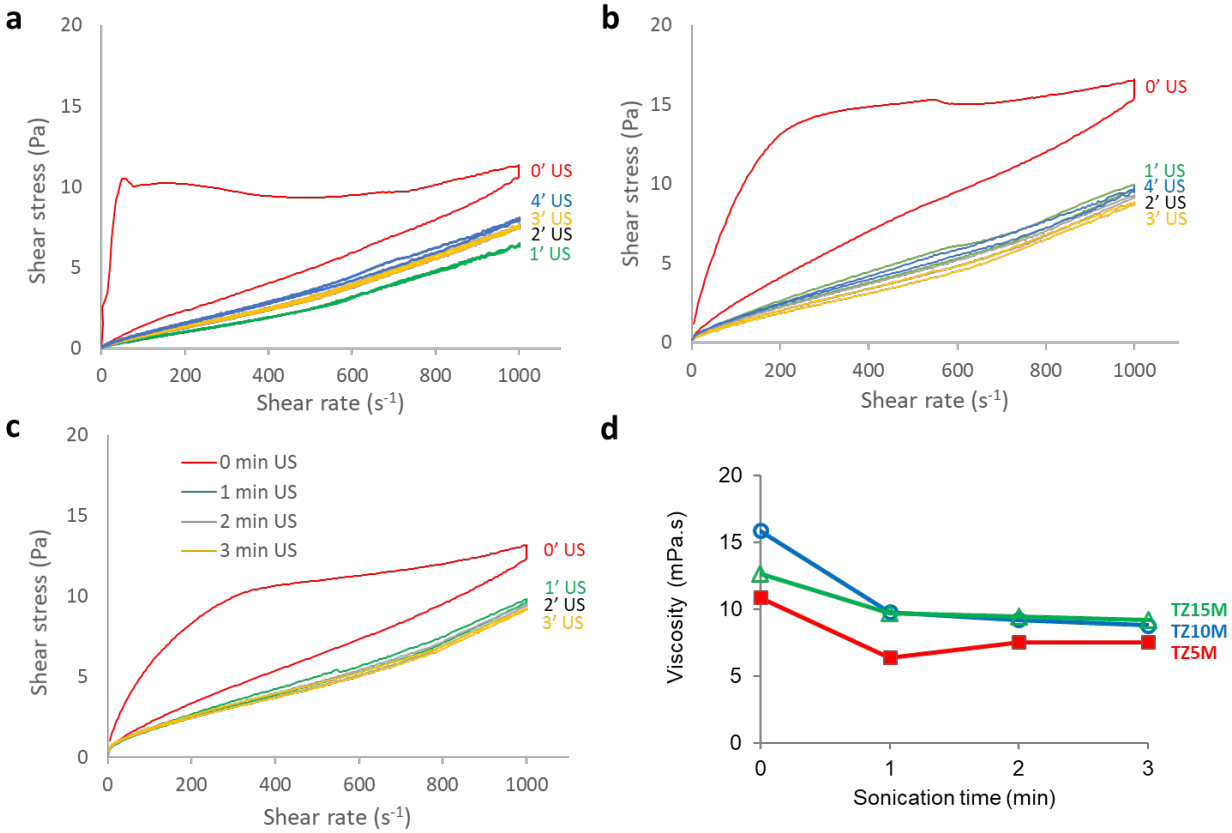

Figure 2. Flow curves of the suspensions TZ5M (a), TZ10M (b) and TZ15M (c) prepared to solids loadings of 30 vol.% dispersed with 0.5 wt% PAA (with regard to TZ4YS) and 1.5 wt% PKV (with regard to $MoSi_2$), and viscosity values as a function of sonication times of the

different slurries at a shear rate of 1000 s^{-1} (d).

3.2 Densification and microstructural characterization

Figure 3 show the piston speed and the displacement curves as a function of sintering temperature of the TZ15M powders mixture corresponding to the sample sintered at 1500 ºC with a soaking time of 5 min.

Firstly, two types of stages can be distinguished corresponding to the piston displacement and piston speed. A first piston displacement occurs at 950 ºC, at which point the sintering process begins and the maximum piston speed is achieved at ~1130 ºC. This first stage stabilizes at 1300 ºC, where the piston speed reaches a minimum. This first intermediate sintering step is carried out without applied pressure and is attributable only to powder compaction of the TZ4YS-$MoSi_2$ mixture. At this point, at 1300 ºC, the pressure of 80 MPa is gradually applied up to 1500 ºC, which leads to the maximum densification of the powder. After 5 minutes of dwell time, the power to the oven was turned off and the oven was allowed to cool naturally.

In the first stage, the increase in deformation of the piston displacement indicates that plastic deformation of $MoSi_2$ powder particles is partially responsible for the initial densification of the TZ4YS-$MoSi_2$ ceramic without pressure applied above the $MoSi_2$ brittle-to-ductile transition upon heating between 900 ºC and 1300 °C [21]. The relative densities of the composites with $MoSi_2$ increased sharply upon application of uniaxial pressure, especially for compositions with high $MoSi_2$ content. Mixture with 15 wt% $MoSi_2$ showed an increase of density ~18% (82% to 99.9%) upon application of pressure from 1300 °C to 1500 °C. The samples with 5 and 10 wt% $MoSi_2$ had a relative density of 99.2% and 99.5%, respectively.

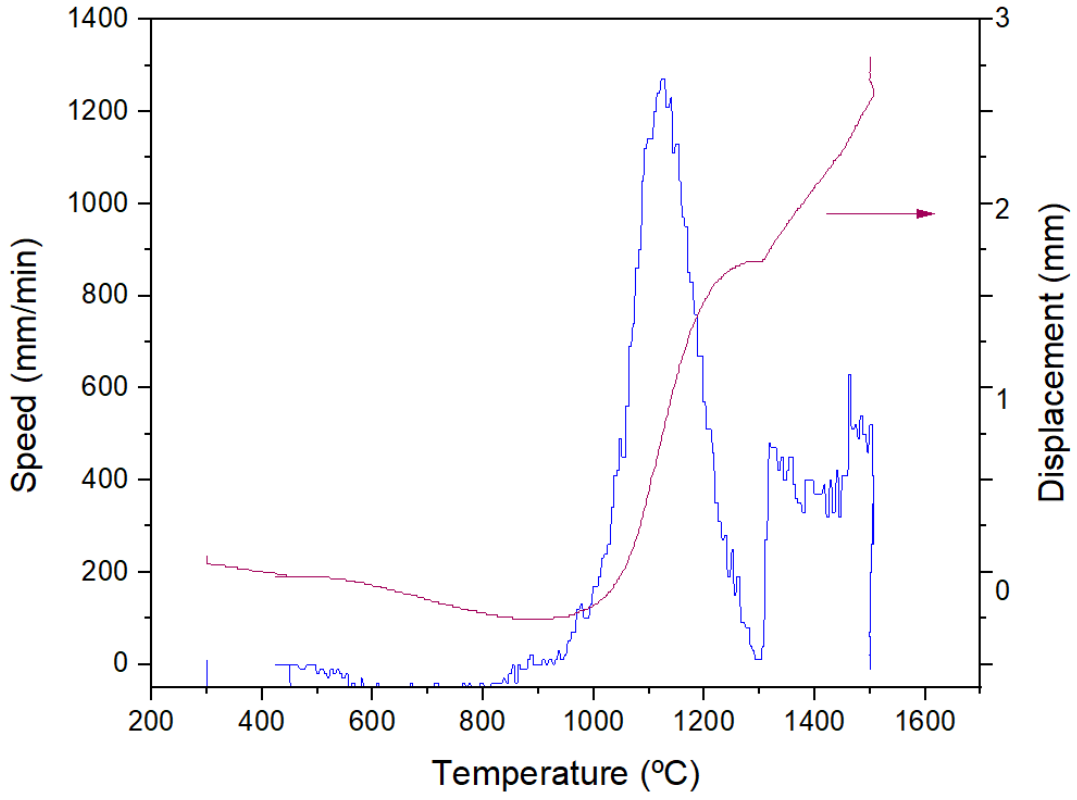

Figure 3. Piston speed and displacement during spark plasma sintering of TZ15M composite at 1500 ºC.

As it can be observed in this second stage of the final sintering regime, the piston speed is stationary and decreased to 0.5 mm/min, and although the shrinkage rate was not dropped to zero, a high densification rate (close to the theoretical density) was achieved avoiding unnecessary decomposition of $MoSi_2$ and overgrowth of the ZrO_2 grain.

The microstructures of typical fracture surfaces of the TZ4YS-$MoSi_2$ composites are shown in Figure 4. The composition, size, distribution and morphology of the grains were analyzed. Porosity evaluated by image analysis on fracture surfaces was found to constitute <0.8 vol.% of TZ5M sample, indicating that the relative density was ≥99.2%. Even lower residual porosity was found for 10 and 15 wt% of $MoSi_2$ compositions, indicating that the relative densities of

those compositions were ≥99.5% and 99.9%, respectively.

Additionally, some differences in the grain sizes can be observed, the $MoSi_2$ varies from 1 to 2 μm while the average grain size of the matrix (ZrO_2) are clearly smaller, 80-100 nm, and this difference will be relevant in the tribological behavior.

This observation suggests that $MoSi_2$ inhibits grain growth of ZrO_2 and enhances densification of the investigated composites. In all samples, the failure of $MoSi_2$ grains occurred because of their inherent brittleness [22].

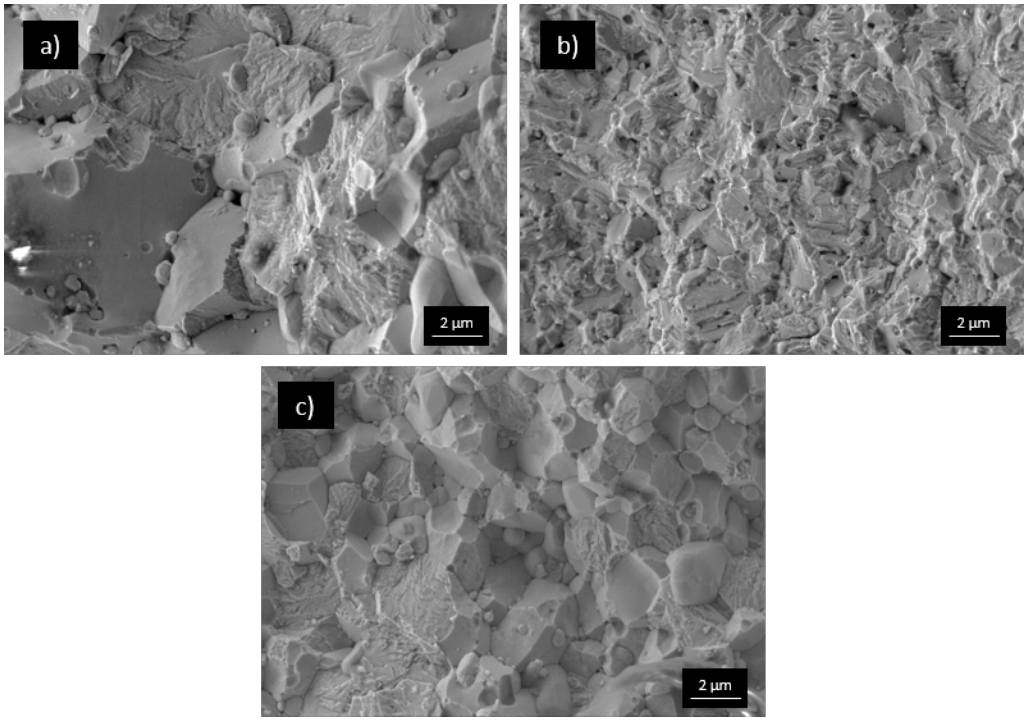

Figure 4. FESEM micrographs of sintered TZ4YS-$MoSi_2$ composites with: (a) 5, (b) 10 and (c) 15 wt% $MoSi_2$.

The EDX elemental mapping of the TZ15M composite corresponding to Figure 4c is shown in Figure 5. A homogeneous distribution of constituent elements of each phase is observed, which indicates that a good control of the physicochemical parameters of powders during colloidal processing.

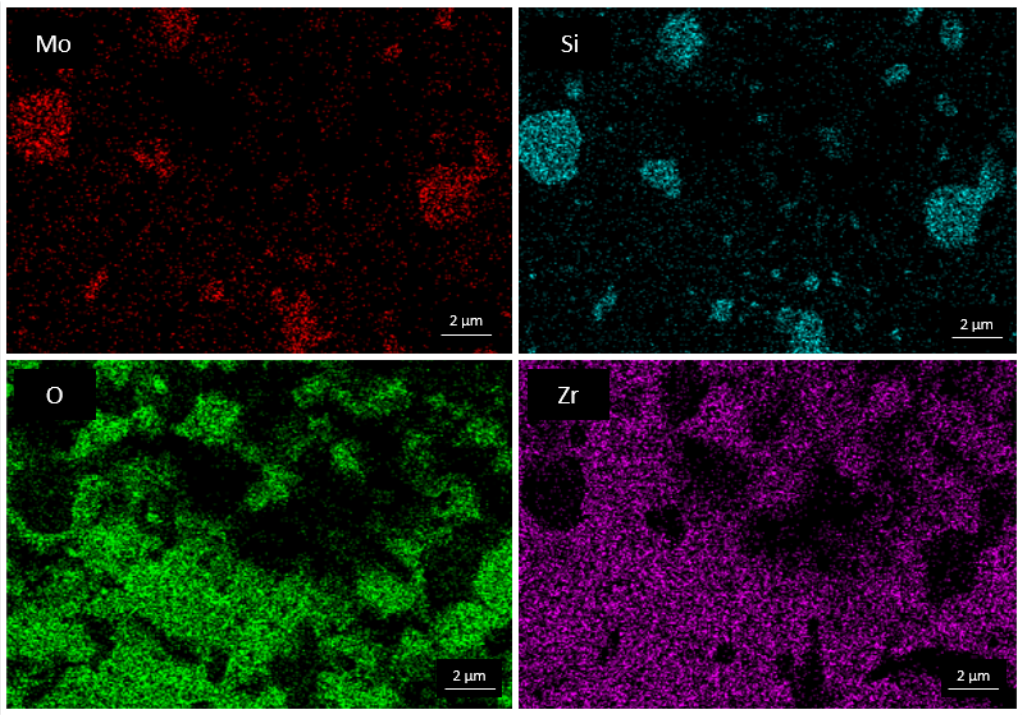

Figure 5. The EDX elemental mapping of Mo, Si, O and Zr of TZ15M composite sintered by SPS.

XRD patterns identifying the constituent phases present in the TZ4YS-$MoSi_2$ composites are shown in Figure 6. The starting powders corresponded to tetragonal ZrO_2 as the main phase, as well as a small contribution of monoclinic ZrO_2 and tetragonal $MoSi_2$.

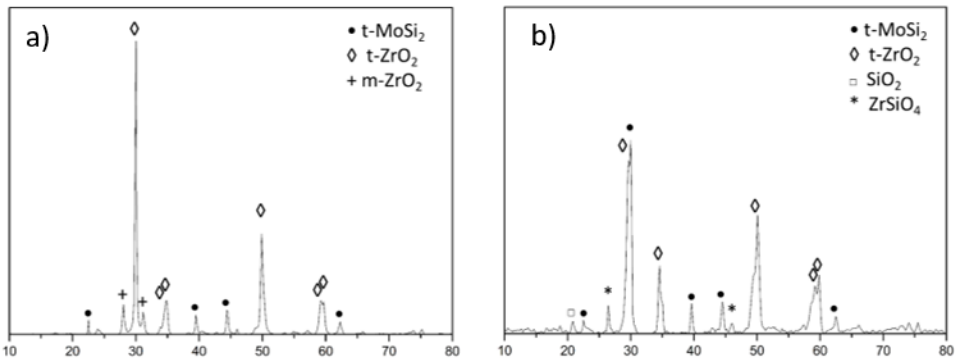

Figure 6. XRD patterns of the TZ15M starting mixture of powders (a) and the composite sintered by spark plasma sintering at 1500 °C (b).

The major phases present in the composite sintered at 1500 ºC are tetragonal phase of ZrO_2 and tetragonal phase of $MoSi_2$. No monoclinic phase of ZrO_2 is observed, because, during the sintering cycle all the monoclinic phase was transformed into tetragonal phase. In addition, some decomposition of $MoSi_2$ occurs, resulting in the formation of new minor phases such as zircon ($ZrSiO_4$), silicon dioxide (SiO_2) and molybdenum trisilicide (Mo_5Si_3).

3.3 Mechanical properties

Mechanical properties as a function of $MoSi_2$ content are summarized in Table 1. The hardness and fracture toughness of TZ4YS monolithic ceramic sintered by SPS at the same conditions, 1500 ºC, were also determined. The values of 14.9 GPa for hardness and 4.9 $MPa \cdot m^{1/2}$ for fracture toughness were obtained. The hardness for the compositions with 5 and 10 wt% $MoSi_2$ is similar (~13 GPa), and an apparent increasing trend in ZT15M associated with its higher densification is observed. However, the fracture toughness values have a clear tendency to increase with $MoSi_2$ content. Maximum fracture toughness (5.4 $MPa \cdot m^{1/2}$) is obtained with the addition of 15 wt% $MoSi_2$. Since all samples have densities near to the theoretical value, the increasing mechanical properties demonstrate a reinforcing effect of $MoSi_2$ related to the fine microstructure. $MoSi_2$ produces a second-phase reinforcement, slightly inhibiting zirconia growth and preventing crack growth, which increases its fracture toughness.

Table 1. Mechanical properties of the TZ4YS-$MoSi_2$ composites obtained by SPS.

Composite	Hardness (GPa)	Fracture Toughness ($MPa \cdot m^{1/2}$)
TZ5M	12.9 ± 0.2	3.7 ± 0.3
TZ10M	13.1 ± 0.1	4.2 ± 0.1

TZ15M	13.5 ± 0.4	5.4 ± 0.3

3.4 Tribological characterization

Several tribological tests were performed on the different samples. The first one was carried out at distances of 1, 5 and 15 m, in order to record the behavior of the materials in the initial stages of wear. The second test was performed at a distance of 2000 m in order to determine whether the steady state is reached or not.

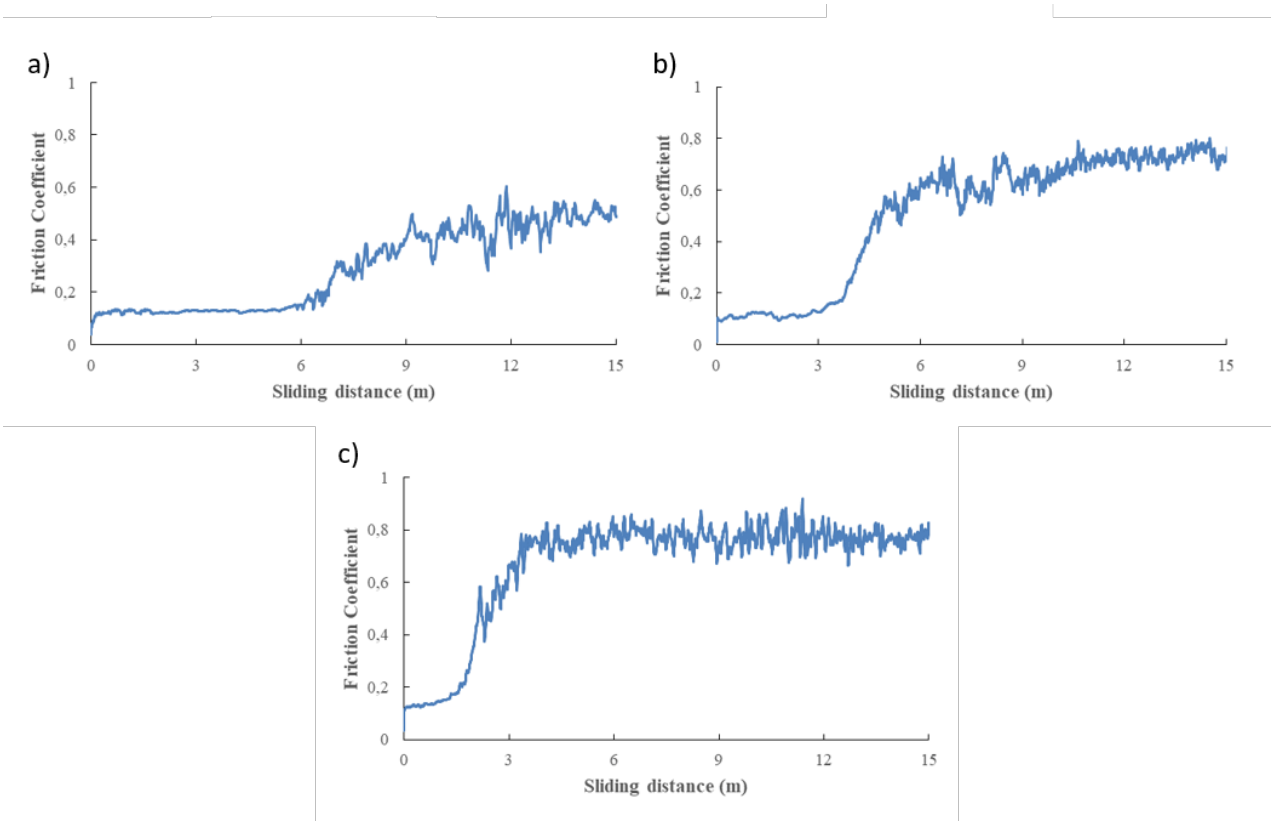

Figure 7. Curves of the friction coefficient evolution with 15 m sliding distance for a) TZ5M, b) TZ10M and c) TZ15M.

Figure 7 shows the coefficient of friction versus sliding distance curves recorded by the pin-on-disk wear test under 15 N for the three composites. It is well known that materials exhibit typical sliding

wear behavior, characterized by an initial slight wear, followed by a transition to severe wear. The coefficient of friction initially starts with a stable value around 0.12 in all cases. However, as the test progresses, there is a sharp increase of the coefficient of friction, which occurs at lower sliding distances as the $MoSi_2$ content increases (after 6 m of sliding for TZ5M, after 4 m for TZ10M and after 2 m for TZ15M samples). This highlights that the $MoSi_2$ content plays an important role in the transition from mild to severe wear. In order to study this transition, the TZ10M sample has been selected, which presents a change in the coefficient of friction at an intermediate distance of 4 m.

Figure 8 shows the wear tracks (detail at high magnification) measured at the end of the tribological test after 1 m (Figure 8a) and 6 m (Figure 8b) of sliding at 15 N of the TZ10M composite. In Figure 8a, the thickness of the wear track measures 113 μm, which coincides with the theoretical Hertz contact zone where the main factors of wear in the first steps with applied load are the elastic modulus, the surface roughness, and the hardness of the materials. In the case of TZ10M sample, the thicknesses of the tracks were measured after 1 m and 6 m, i.e. before and after transition to severe wear, and the percentual increase in the thickness of the track was ~42%. In the other compositions, TZ5M and TZ15M, the percentual increase in the thicknesses of the tracks were ~67% and ~29%, respectively. These data evidence that the higher the $MoSi_2$ content, the earlier the transition to severe wear occurs and the smaller the track produced. Although the $MoSi_2$ content did not significantly modify the hardness of the compacts, it does modify their tribological behavior in the first few meters.

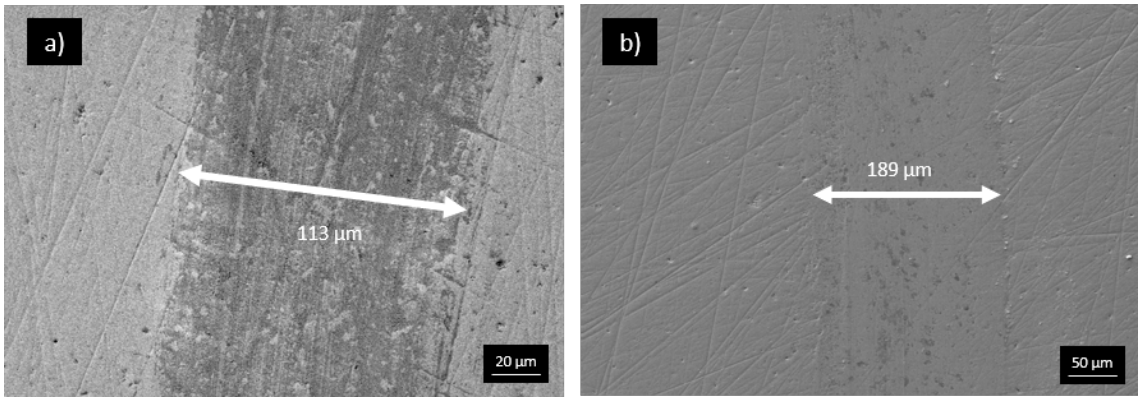

Figure 8. FESEM micrographs: a) 1 m and b) 6 m wear tracks test on the TZ10M composite sintered by SPS at 1500 ºC.

The transition from light to severe wear occurs at some critical sliding distance as a result of grain cracking and loosening, whereby the transition is governed by plastic deformation due to increased dislocation density at grain boundaries [23]. As the test progresses, other factors intervene, such as yield strength, toughness, localized temperature, third body particles, among others [24]. Coronado et al. [25] explain that there is a relationship between the increase in wear rate and the ratio of the abrasive medium and the hardness of the test specimen. If the hardness of the abrasive is 1.9 times lower than that of the test sample the increase in wear is significant, in our case, the difference in hardness between the three composites is negligible so the ratio remains almost at 1.44. This could be the reason why at the end of the test the wear rate is almost the same, despite the slight difference between the friction coefficients, as can be seen below.

When the friction coefficient arises the steady state, damage to the contact surfaces begins to be noticeable as can be seen in Figure 9. It is perceptible how plasticization becomes part of the tribological process as well as a fish scale pattern, roller like particles and plasticized zones.

Damage at 15 m sliding becomes severe, as reflected in Figure 9b, where grain cracking and loosening is clearly appreciated, demonstrating that the larger the contact stresses and the deeper penetration by abrasive particles enhance the damage. The wear mechanisms are dominated by the

fracture process mainly in the pin (Al_2O_3 ball), and pull-out of particles from the third body as explained by Mukhopadhyay and Mai [26].

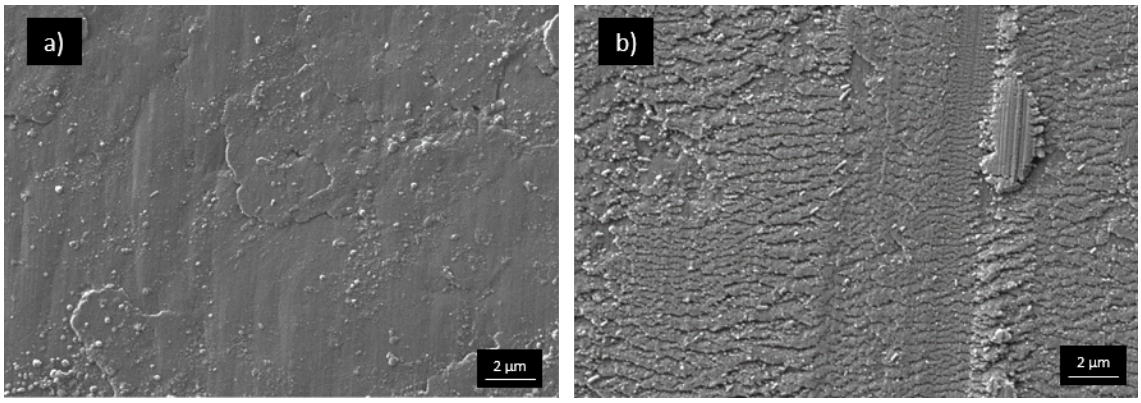

Figure 9. FESEM micrographs: a) 6 m sliding wear tracks and b) 15 m sliding detail of TZ10M composite sintered by SPS at 1500 ºC.

A great difference between a short-term test (Figure 7) and a long-distance test (Figure 10) is noticeable. A great shift in the frictional coefficient is manifested as can be seen on Table 2.

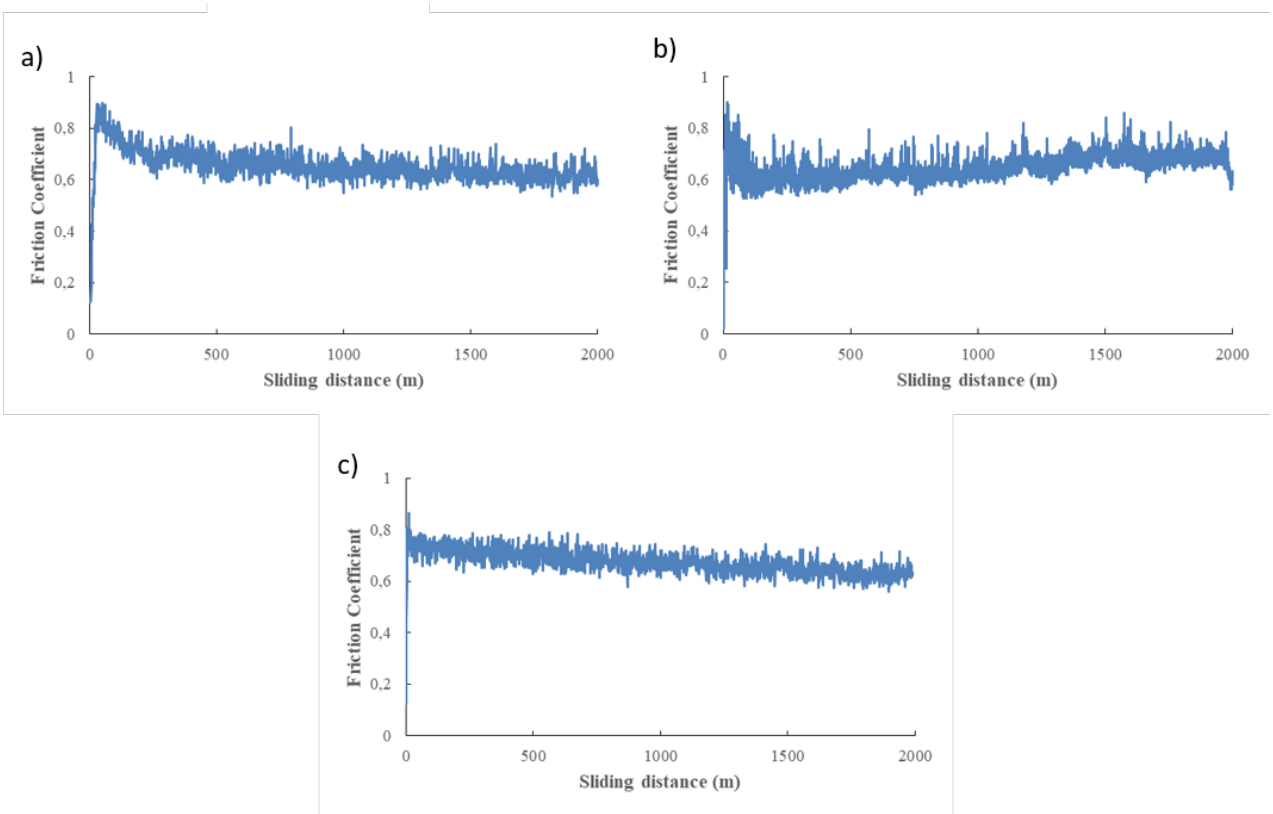

Figure 10. Curves of the friction coefficient evolution with 2000 m sliding distance for the: a) TZ5M, b) TZ10M and c) TZ15M.

Table 2. Frictional parameters of TZ4YS-$MoSi_2$ composites.

	TZ5M	TZ10M	TZ15M
Friction coefficient average (mild wear)	0.13	0.12	0.13
Friction coefficient range (mild wear)	0.04	0.08	0.04
Transition period (m)	6	4	2
Friction coefficient average (steady state)	0.64	0.65	0.68
Friction coefficient range (steady state)	0.24	0.30	0.22

As mentioned above, the $MoSi_2$ content plays an important role in the mild to severe transition period and less significance in a long-distance wear behaviour. In the case of the friction coefficient average in the steady state, the $MoSi_2$ content results in an increase in the friction coefficient, although this variation was less accentuated. An increase in $MoSi_2$ content from 5 to 10 wt% implies an increase of 0.7% in the friction coefficient, if the content is 15 wt%, the increase is 5.4%. Wang et al. claim that the hardness appears to have the greatest influence on the overall sliding-wear since it controls the initial mild wear and sets the subsequent cumulative wear degradation [27].

On the other hand, Dogan and Hawk [28] suggest that the differences in wear behavior should be a consequence of toughening mechanisms. The tribosurface generated in the first two meters change dramatically in few meters more as can be seen on Figures 8 and 9, where a beginning of a galling

process is advised at 15 m sliding. TZ10M composite shows a surface with a mild to severe wear mechanism, on which the concentrated stresses on a tribological layer result in plastic deformation, as described by Wang and Hsu [29]. The surface shows a tribofilm plasticized with smeared morphology with parallel cone cracks. Additionally, a plastic distorted abrasive grove is evident. Two main wear mechanisms are observed in Figure 9b, a plastic smearing and an adhesive tearing. The plastic smearing corresponded to a lower friction coefficient in the beginning of the test, while adhesive tearing corresponded to higher values after few meters. The adhesive tearing caused much more wear than plastic smearing as described by Jin and Yang [30].

Figure 11 shows the erosion surface of the TZ10M composite and the EDX analysis of a selected area (square). It can be seen how the surface forms symmetrical grooves of ~140 μm along the width of the analyzed track. The width of the wear track is ~1750 μm.

The $MoSi_2$ particles, which were subjected to large contact stresses, appear fractured and smeared and stick on the surface to form an Al_2O_3-$MoSi_2$ debris mixture as seen on FESEM-EDX elemental mapping of the tribosurface of a TZ10M composite in a 2000 m test, where fine particles of $MoSi_2$ are mixed with the Al_2O_3 transferred to the composite surface.

Additionally, as can be observed in Figure 11 shallow abrasion grooves are produced within these smooth regions. According to Michalak et al. [31] this change is responsible of the frictional coefficient increase. Dogan and Hawk [28] pointed out that the differences in wear behavior of brittle materials should be a consequence of the nature of toughening mechanisms.

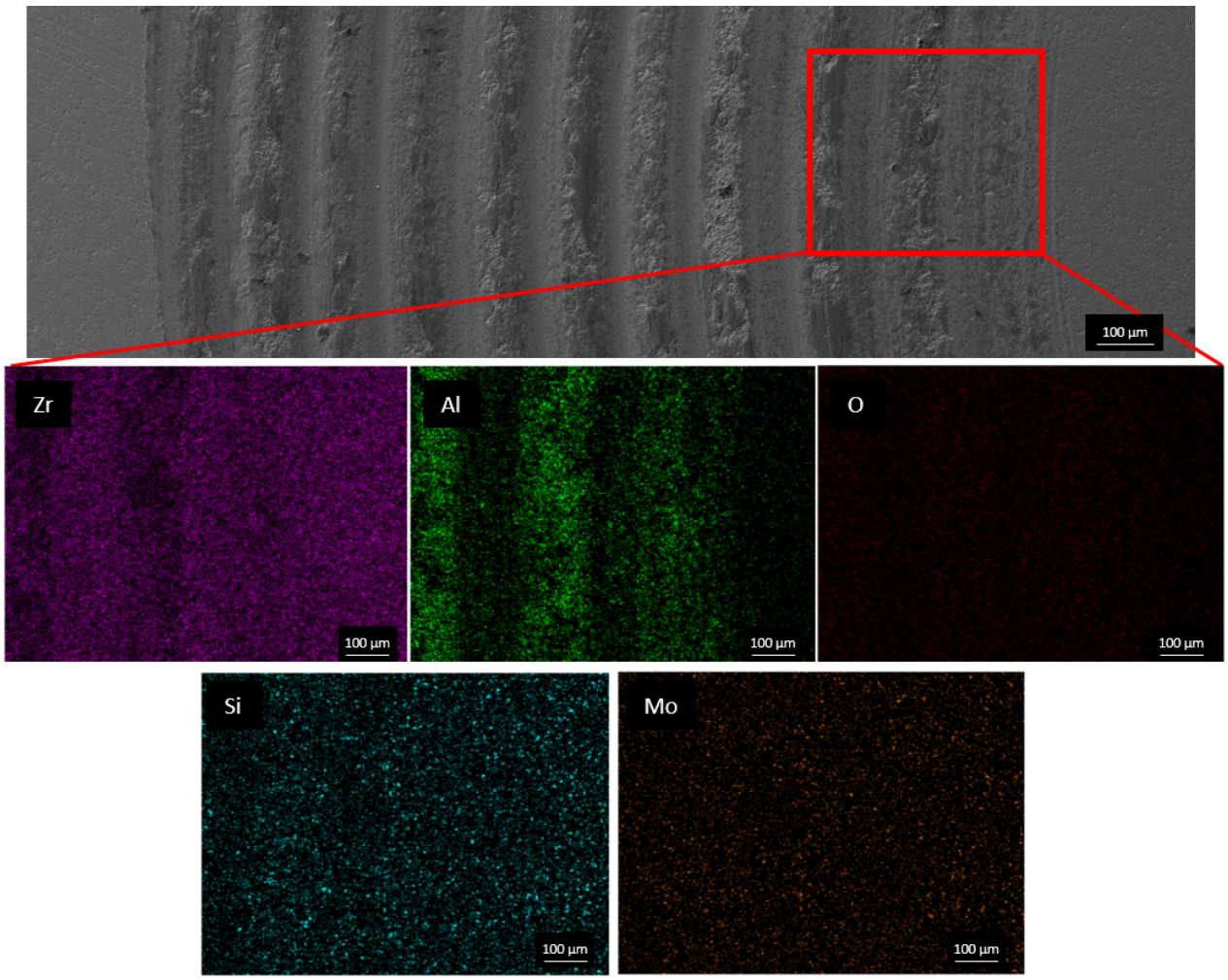

Figure 11. Wear track after 2000 m sliding of TZ10M composite sintered by SPS at 1500 ºC.

Figure 12 shows the surface of Al_2O_3 ball post 2000 m sliding on TZ4YS-10$MoSi_2$ composite. It is possible to deduce that the striation is a mixture of Al_2O_3 and TZ4YS-$MoSi_2$ particles. This amalgam erodes the ball, and the ball debris and the fractured TZ4YS-$MoSi_2$ from the specimen are plasticized and adhered in the borders creating a new striation, so the formation of striation-groove-striation grows symmetrically from center to borders.

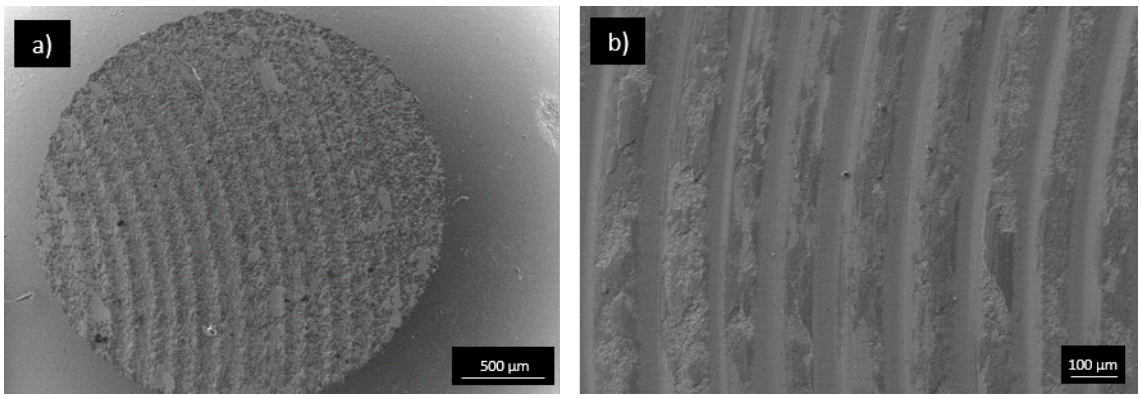

Figure 12. Low (a) and high magnification (b) pictures of the Al_2O_3 ball cross-section after 2000 m sliding on TZ10M sintered composite.

Conclusions

The conclusions that can be reached from this study of mechanical and tribological properties the TZ4YS-$MoSi_2$ composites are as follows:

- The mechanical properties increase with increasing $MoSi_2$ percentage. The degree of densification achieved by SPS at 1500 ºC is >99% T.D.

- The $MoSi_2$ content was associated to the beginning of the transition mild to severe wear, higher the amount of $MoSi_2$ faster is the transition. The short-term wear behavior exhibits a nearly steady frictional coefficient around 0.12 in all specimens. This behavior was correlated with $MoSi_2$ content which aids the formation of a tribolayer.

- Two main wear mechanisms were observed, the plastic smearing corresponded to a lower friction coefficient in the beginning of the test, while adhesive tearing corresponded to higher values after few meters.

- The TZ4YS-$MoSi_2$ particles, which were subjected to large contact stresses, were fractured, smeared and stick on the surface to form an Al_2O_3 and TZ4YS-$MoSi_2$ debris mixture which adheres at border of the contact zone. The formation of striation-groove pattern grows symmetrically from center of the Al_2O_3 ball to borders.

Acknowledgments

The authors would like to thank the Ministry of Science, Innovation and Universities (Spain) for its financial through the projects RTI2018-099033-B-C32&C33 (MCIU/AEI/FEDER, UE) and RYC-2016-20915.

Refereces

[1] B. Basu, K. Balani, Advanced structural ceramics, John Wiley & Sons, 2011.

[2] S. Tailor, R. Mohanty, D. A., Development of a new TBC system for more efficient gas turbine engine application, Mater. Today Proc. 3 (2016) 2725–2734. https://doi.org/10.1016/J.MATPR.2016.06.019.

[3] A. Borrell, M.D. Salvador, Advanced ceramic materials: processed and applications, Ed. UPV, 2018.

[4] N. Eliaz, Degradation of implant materials, Springer Science & Business Media, 2012.

[5] F. Nozahic, D. Monceau, C. Estournès, Thermal cycling and reactivity of a $MoSi_2/ZrO_2$ composite designed for self-healing thermal barrier coatings, Mater. Des. 94 (2016). https://doi.org/10.1016/j.matdes.2016.01.054.

[6] R.J. Grohsmeyer, L. Silvestroni, G.E. Hilmas, F. Monteverde, W.G. Fahrenholtz, A. D'Angió, D. Sciti, ZrB2-MoSi2 ceramics: A comprehensive overview of microstructure and properties relationships. Part I: Processing and microstructure, J. Eur. Ceram. Soc. 39 (2019) 1939–1947. https://doi.org/https://doi.org/10.1016/j.jeurceramsoc.2019.01.022.

[7] J. Yan, Z. Zhang, L. Liu, H. Xu, Z. Mao, Effect of Nano-ZrO2 on the Microstructure and High Temperature Tribological Properties of $MoSi_2$ Coating, J. Therm. Spray Technol. 22 (2013) 873–881. https://doi.org/10.1007/s11666-013-9924-9.

[8] J. Meng, J. Lu, J. Wang, S. Yang, Tribological Behavior of $MoSi_2$ and Its Composites in Sliding Against Ni-Based Alloys, Tribol. Lett. 16 (2004) 37–42. https://doi.org/10.1023/B:TRIL.0000009712.77946.55.

[9] B. Núñez-González, A. Ortiz, F. Guiberteau, N. Padture, Effect of $MoSi_2$ content on the lubricated sliding-wear resistance of ZrC–$MoSi_2$ composites, J. Eur. Ceram. Soc. 31 (2011) 877–882. https://doi.org/10.1016/j.jeurceramsoc.2010.11.017.

[10] L. Micele, G. Palombarini, S. Guicciardi, L. Silvestroni, Tribological behaviour and wear resistance of a SiC–$MoSi_2$ composite dry sliding against Al_2O_3, Wear. 269 (2010) 368–375. https://doi.org/https://doi.org/10.1016/j.wear.2010.04.021.

[11] L. Zhang, Z. Tong, R. He, C. Xie, X. Bai, Y. Yang, D. Fang, Key issues of $MoSi_2$-UHTC ceramics for ultra high temperature heating element applications: Mechanical, electrical, oxidation and thermal shock behaviors, J. Alloys Compd. 780 (2019) 156–163.

[12] J. Kuchino, K. Kurokawa, T. Shibayama, H. Takahashi, Effect of microstructure on oxidation resistance of $MoSi_2$ fabricated by spark plasma sintering, Vacuum. 73 (2004) 623–628.

[13] R. Moreno, Better ceramics through colloid chemistry, 40 (2020) 559–587.

[14] T.R. Paul, M.K. Mondal, M. Mallik, Microstructure dependent physical and mechanical properties of spark plasma sintered ZrB_2-$MoSi_2$–SiCw composites, Int. J. Refract. Met. Hard Mater. 79 (2019) 131–137.

[15] A. Borrell, L. Navarro, C.F. Gutiérrez-González, C. Alcázar, M.D. Salvador, R. Moreno, Microstructure and mechanical properties of 4YTZP-SiC composites obtained through colloidal processing and Spark Plasma Sintering, Bol. Soc. Esp. Ceram. Vidr. 60 (2021) 175–182.

[16] ASTM C373-88. Standard Test Method for Water Absorption, Bulk Density, Apparent Porosity, and Apparent Specific Gravity of Fired Whiteware Products., ASTM Int. West

Conshohocken, PA, 1988.

[17] ASTM E384–17. Standard Test Method for Microindentation Hardness of Materials, ASTM Int. West Conshohocken, PA, 2017.

[18] K. Niihara, R. Morena, D.P.H. Hasselman, Evaluation ofK Ic of brittle solids by the indentation method with low crack-to-indent ratios, J. Mater. Sci. Lett. 1 (1982) 13–16.

[19] ASTM G99–17. Standard Test Method for Wear Testing with a Pin-on-Disk Apparatus., ASTM Int. West Conshohocken, PA, 2020.

[20] V.L. Popov, M. Heß, E. Willert, Handbook of contact mechanics: exact solutions of axisymmetric contact problems, Springer Nature, 2019.

[21] S.R. Srinivasan, R.B. Schwarz, J.D. Embury, Ductile-to-brittle transition in $MoSi_2$, MRS Online Proc. Libr. Arch. 288 (1992).

[22] R. He, Z. Tong, K. Zhang, D. Fang, Mechanical and electrical properties of $MoSi_2$-based ceramics with various ZrB_2-20 vol% SiC as additives for ultra high temperature heating element, Ceram. Int. 44 (2018) 1041–1045.

[23] O. Borrero-López, A.L. Ortiz, F. Guiberteau, N.P. Padture, Microstructural design of sliding-wear-resistant liquid-phase-sintered SiC: an overview, J. Eur. Ceram. Soc. 27 (2007) 3351–3357.

[24] M. Kalin, Influence of flash temperatures on the tribological behaviour in low-speed sliding: a review, Mater. Sci. Eng. A. 374 (2004) 390–397.

[25] J.J. Coronado, S.A. Rodríguez, A. Sinatora, Effect of particle hardness on mild–severe wear transition of hard second phase materials, Wear. 301 (2013) 82–88.

[26] A.K. Mukhopadhyay, M. Yiu-Wing, Grain size effect on abrasive wear mechanisms in alumina ceramics, Wear. 162 (1993) 258–268.

[27] Q. Wang, C. Ramírez, C.S. Watts, O. Borrero-López, A.L. Ortiz, B.W. Sheldon, N.P.

Padture, Fracture, fatigue, and sliding-wear behavior of nanocomposites of alumina and reduced graphene-oxide, Acta Mater. 186 (2020) 29–39.

[28] C.P. Doğan, J.A. Hawk, Role of zirconia toughening in the abrasive wear of intermetallic and ceramic composites, Wear. 212 (1997) 110–118.

[29] Y. Wang, S.M. Hsu, Wear and wear transition mechanisms of ceramics, Wear. 195 (1996) 112–122.

[30] Y. Jin, Y. Yang, Tribological behavior of various plasma-sprayed ceramic coatings, Surf. Coatings Technol. 88 (1997) 248–254.

[31] M. Michalak, L. Latka, P. Sokolowski, F.-L. Toma, H. Myalska, A. Denoirjean, H. Ageorges, Microstructural, mechanical and tribological properties of finely grained Al_2O_3 coatings obtained by SPS and S-HVOF methods, Surf. Coatings Technol. 404 (2020) 126463.